Relaxation in Spherical Coordinates: Analysis and Optimization of pseudo-SSFP based MR-Fingerprinting

Jakob Assländer[1,2], Riccardo Lattanzi[1,2,3], Daniel K Sodickson[1,2,3] and Martijn A Cloos[1,2]

[1] Bernard and Irene Schwartz Center for Biomedical Imaging, Department of Radiology, New York University School of Medicine, New York, NY, USA

[2] Center for Advanced Imaging Innovation and Research (CAI^{2}R), Department of Radiology, New York University School of Medicine, New York, NY, USA

[3] The Sackler Institute of Graduate Biomedical Sciences, New York University School of Medicine, New York, NY, USA

March 3, 2017

Submitted to *Magnetic Resonance in Medicine*

arXiv:1703.00481v1 [physics.med-ph] 1 Mar 2017

Abstract

Purpose

This work analyses relaxation in balanced pseudo steady-state free precession sequences (pSSFP) and provides an optimal control framework to optimize MR-Fingerprinting sequences with respect to noise in the T_1- and T_2-maps.

Method

The Bloch equations were reformulated in spherical coordinates and numerical optimizations of the excitation pattern were performed based on the Cramér-Rao bound. The performance of resulting patterns was tested with simulations, as well as in vivo experiments in the human brain.

Results

In a representative optimization, the Cramér-Rao bound for T_2 was reduced by 67%, which translated into a noise reduction of 42% measured in vivo compared to the original pSSFP sequence. At the same time, the noise level in T_1 remained approximately constant. The sequence was optimized for reduced noise at a single set of relaxation times. Nevertheless, good performance was observed over a broad spectrum of relaxation times. Further, the smooth shapes of the optimized spin trajectories provide a basis for the analysis of the encoding process of relaxation times for parameter mapping and beyond.

Conclusion

The proposed optimization framework is robust and provides simple, flexible and physically interpretable excitation patterns with superior noise performance.

Introduction

The dynamics of large spin-1/2 ensembles in a magnetic field can be described using the Bloch equations, which capture the macroscopic effects of spin-lattice and spin-spin interactions with the characteristic time constants T_1 and T_2, respectively. The exponential behavior of T_1 relaxation makes a series of inversion-recovery experiments a natural choice for quantitative T_1 mapping. Similarly, a series of spin echo experiments with varying echo times provides an intuitive way to measure T_2. Besides these methods, which effectively strive to trace exponential relaxation curves following a single perturbation from thermal equilibrium, both T_1 and T_2 can also be estimated by measuring magnetization in various steady-state conditions (1, 2, 3, 4). These methods are more time efficient, because the magnetization no longer needs to be fully relaxed before each measurement. By forgoing analytic solutions, a richer sequence design space becomes available, which allows even faster quantitative measurements (5). This strategy, called MR-Fingerprinting (MRF), provides a framework to generalize parameter mapping. As a model-based method that matches the signal evolution to a precomputed dictionary, MRF provides the freedom to design optimized pulse sequences that rely neither on an exponential signal evolution nor on a steady-state condition. Further, MRF allows one to model the spin physics in biological tissue more accurately by including chemical exchange (6) or by incorporating hampering factors like B_0- (5) and B_1-inhomogeneities (7, 8). Overall, MRF offers a promising route to accurate and reliable quantitative parameter mapping.

The original MRF publication (5) used a balanced steady-state free precession (SSFP) based sequence with a heuristic, smooth flip angle pattern, perturbed by small pseudo-random variations. For a purely random flip angle pattern, Davies et al. found that the length of the excitation pattern must scale with the square of the undersampling factor in each time frame in order to achieve the same reconstruction performance (Eq. [4.8] in Ref. (9)). In other words, repeating the exact same excitation pattern twice with a different k-space trajectory or quadrupling the length of a random sequence has the same effect. This illustrates the inefficiency of random flip-angle patterns.

In this work, we propose a method to optimize the flip-angle pattern for pseudo steady-state free precession (pSSFP) (10) based MRF sequences. First, we recast the Bloch equations in spherical coordinates, which allows us to describe the spin dynamics of the pSSFP sequence with a single first order differential equation. We show that all relaxation processes occur in the radial direction, while the radio frequency (RF) pulses affect exclusively the polar angle, which indirectly influences the relaxation. Within this framework, we can, thus, view the polar angle as a control of the relaxation process and we can use the rich optimal control framework (11, 12) to optimize the pulse sequence. Employing the Cramér-Rao bound as a figure of merit, the optimization robustly convergences to RF-patterns that can be easily interpreted on the Bloch-sphere and that provide considerably improved noise performance as compared with unoptimized patterns.

Theory

The Bloch Equations in Spherical Coordinates

We can normalize the Bloch equation to have a magnetization of $\mathbf{M}_0 = (x_0, y_0, z_0) = (0, 0, 1)$ at thermal equilibrium. In Cartesian coordinates the normalized Bloch equations read

$$\dot{x} = \omega_z \cdot y - \omega_y \cdot z - \frac{x}{T_2} \quad [1]$$

$$\dot{y} = \omega_x \cdot z - \omega_z \cdot x - \frac{y}{T_2} \quad [2]$$

$$\dot{z} = \omega_y \cdot x - \omega_x \cdot y + \frac{1 - z}{T_1}. \quad [3]$$

Here, $x(t), y(t)$ are the two components of the transversal magnetization, while $z(t)$ denotes the longitudinal component and $\dot{x}(t), \dot{y}(t), \dot{z}(t)$ are their temporal derivatives. The real and imaginary part of the RF-pulses are given by $\omega_x(t)$ and $\omega_y(t)$, while $\omega_z(t)$ denotes the Larmor frequency. The notation of the temporal dependency of variables is omitted here for improved readability.

Spherical coordinates are defined by $x = r \sin\vartheta \cos\varphi$, $y = r \sin\vartheta \sin\varphi$ and $z = r \cos\vartheta$, where r is the radius, ϑ the polar angle or the angle between the magnetization and the z-axis and φ is the azimuth or the angle between the x-axis and the projection of the magnetization onto the x-y-plane. Thermal equilibrium is given by $r_0 = 1$, $\vartheta_0 = 0$ and $\varphi_0 = 0$, where the latter can be chosen freely. The Bloch equations in spherical coordinates read

$$\dot{r} = \frac{\cos\vartheta - r\cos^2\vartheta}{T_1} - \frac{r\sin^2\vartheta}{T_2} \quad [4]$$

$$\dot{\vartheta} = \frac{\sin\vartheta}{T_1}\left(\cos\vartheta - \frac{1}{r}\right) - \frac{\cos\vartheta \sin\vartheta}{T_2} + \omega_x \sin\varphi - \omega_y \cos\varphi \quad [5]$$

$$\dot{\varphi} = \cot\vartheta \left(\omega_y \sin\varphi + \omega_x \cos\varphi\right) - \omega_z. \quad [6]$$

One can observe that r does not explicitly depend on RF-pulses and the Larmor frequency. The only way to manipulate r is via relaxation processes, which depend on ϑ. The polar angle ϑ explicitly depends on the RF-pulses as well as relaxation, while φ explicitly depends on the Larmor frequency and the RF-pulses, but is not affected by relaxation. Throughout the remainder of this manuscript, we use the Bloch equations to describe the magnetization in a rotating frame of reference, such that ω_z denotes the off-resonance frequency.

The Bloch Equations for pseudo-SSFP Sequences

Traditional SSFP sequences consist of a train of equidistant RF-pulses with a constant flip angle and a phase increment of π in consecutive pulses. This leads to a refocusing of all magnetization within a passband at the echo time $TE = TR/2$ (13). pSSFP generalizes the spin echo nature of SSFP sequences for varying flip angles (10). To achieve a pseudo steady-state, three conditions need to be fulfilled: In order to invert the phase slope of the magnetization, all RF-pulses need to flip the magnetization such that the sign of ϑ changes. The second pSSFP condition defines a relation between varying TR and TE based on the

evolution of ϑ, while the third conditions scales *TR* and *TE* ensuring that the dephasing of a single passband is limited to $-\pi/2 \leq \varphi < \pi/2$ throughout the entire experiment. Therefore, we use the limits $-1 \leq r(t) \leq 1$, $-\pi/2 \leq \vartheta(t) \leq \pi/2$ and $-\pi/2 \leq \varphi < \pi/2$ to uniquely define the spherical coordinate system in this paper. A mathematical formulation of the pSSFP conditions are given by Eqs. [1], [5] and [7] in Ref. (10).

For the special case of pSSFP sequences (10), the Bloch equation in spherical coordinates can be simplified. We assume all voxels' spin isochromats to lie within the on-resonant passband. More precisely, we assume $TR \ll \pi/|\omega_z|$ to be fulfilled for all isochromats. However, this assumption can be extended to off-resonant passbands e.g. by describing the magnetization in a different rotating frame of reference. Under this assumption, we can exploit the spin echo nature of pSSFP sequences to neglect dephasing and we can assume $\omega_z = 0$. Without loss of generality, we can assume the RF-pulses to be aligned with the y-axis, which implies $\omega_x = 0$. Starting from the above defined thermal equilibrium ($\varphi_0 = 0$), the Eqs. [5] and [6] can be simplified to

$$\dot{\vartheta} = \frac{\sin\vartheta}{T_1}\left(\cos\vartheta - \frac{1}{r}\right) - \frac{\cos\vartheta\sin\vartheta}{T_2} - \omega_y \qquad [5']$$

$$\dot{\varphi} = 0. \qquad [6']$$

If we use Eqs. [4], [5'] and [6'] to describe magnetization that departs from thermal equilibrium by a combination of an inversion and an excitation pulse and relaxes freely thereafter ($\omega_y = 0$), the magnetization follows a trajectory as sketched in Fig. 1a. However, pSSFP sequences necessitate the magnetization to change the sign of ϑ in consecutive *TR*. Enforcing this behavior by RF-pulses entails a vanishing relaxation along the polar angle when averaged over multiple *TR* (see Appendix). Fig. 1b illustrates this effect for an SSFP sequence with an RF-train with a constant flip angle and an alternating phase. As already shown by Hennig et al. (14), the SSFP pattern forces the magnetization onto a cone with the angle $\vartheta = \alpha/2$, where α denotes the flip angle.

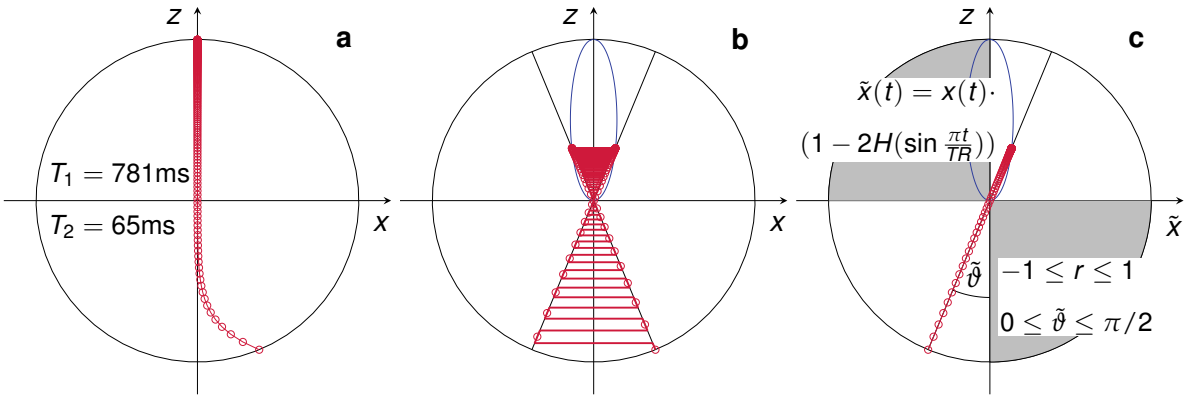

Figure 1: The dynamics of white matter magnetization during free relaxation is depicted in (a). Note that the trajectory was calculated with Eqs. [4], [5'] *and* [6'], *which neglect off-resonance effects. Thus, this spin dynamics is a mere gedankenexperiment providing an analogy to the spin dynamics of the inversion-recovery SSFP sequence shown in (b). Here, the oscillating RF-pulses force the magnetization onto a cone on which it relaxes until it reaches the steady-state ellipse (blue). In an oscillating frame of reference, the same relaxation induced spin dynamics purely takes place along the radial direction (c).*

To simplify the description of the spin dynamics even further, we can switch to an oscillating frame of reference defined by $\tilde{\vartheta}(t) = \vartheta(t) \cdot (1 - 2 \cdot H(\sin(\pi \cdot t/TR)))$, where H is the Heaviside function. In this frame of reference, a changing sign of ϑ in consecutive TR can be enforced implicitly by the limit $0 \leq \tilde{\vartheta} \leq \pi/2$. The spin dynamics in the oscillating frame of reference is illustrated in Fig. 1c.

Due to the absence of relaxation along the polar coordinate, $\tilde{\vartheta}$ is merely determined by the RF-pulses, and the spin dynamics can be described by a single first order differential equation:

$$\dot{r}(t) = \frac{\cos\tilde{\vartheta}(t) - r(t)\cos^2\tilde{\vartheta}(t)}{T_1} - \frac{r(t)\sin^2\tilde{\vartheta}(t)}{T_2}, \qquad [7]$$

which is independent of TR within the limit $TR \ll \{T_1, T_2\}$ and assuming the function $\tilde{\vartheta}(t)$ changes slowly compared TR (see Appendix). Further, Eq. [A5] in the Appendix demonstrates that the spin dynamics in Eq. [7] depends merely on the relative, dimensionless variables T_1/T_2 and t/T_2.

Methods

Cramér Rao Bound

There are many different aspects of the MRF pulse sequence design that provide interesting opportunities for improvement. A complete analysis of all these parameters simultaneously is currently out of reach. Instead, this work will focus on the analysis and optimization of the T_1- and T_2-encoding power of the RF-pulse train in pSSFP pulse sequences, independent from the specific k-space trajectory or undersampling factor that may be used in the imaging sequence. To this end, the Cramér-Rao bound will be used to provide a universal limit for the noise variance of the estimated parameters. Given an unbiased estimator, i.e. the algorithm used to calculate the proton density (PD), T_1 and T_2, the variance of these parameters is at least as big as the corresponding Cramér-Rao lower bound.

The Cramér-Rao bound is calculated by numerically solving Eq. [7]. Note that the temporal discretization can be chosen freely, since Eq. [7] is independent of TR. In discretized notation, the Cramér-Rao bound is defined by the inverse of the Fisher information matrix $\mathbf{F} \in \mathbb{R}^{3\times3}$ with the entries $\mathbf{F}_{i,j} = \mathbf{b}_i^T\mathbf{b}_j/\sigma^2$ given by

$$\mathbf{b}_1 = d\tilde{\mathbf{x}}/dPD = \tilde{\mathbf{x}} \qquad [8]$$

$$\mathbf{b}_2 = d\tilde{\mathbf{x}}/dT_1 \qquad [9]$$

$$\mathbf{b}_3 = d\tilde{\mathbf{x}}/dT_2. \qquad [10]$$

Here $\tilde{\mathbf{x}} \in \mathbb{R}^{N_t}$ is a vector describing the measured signal, or, equivalently, the transversal magnetization at N_t discrete time points, and σ^2 is the input variance. Each element of the vector is given by $\tilde{x}_n = r(t_n) \cdot \sin\tilde{\vartheta}(t_n)$. The vectors $\mathbf{b}_i$ describe the derivatives of the signal evolution with respect to all considered parameters. Note that the normalization $r_0 = 1$ implies that the proton density is normalized as well ($PD = 1$). Therefore, PD can be omitted in all equations and $d\tilde{\mathbf{x}}/dPD = \tilde{\mathbf{x}}$ holds true.

By normalizing with the input variance σ^2 and the relaxation time, we can define the

relative Cramér-Rao bounds to be

$$rCRB(PD) = \frac{(\mathbf{F}^{-1})_{1,1}}{\sigma^2} \quad [11]$$

$$rCRB(T_1) = \frac{(\mathbf{F}^{-1})_{2,2}}{\sigma^2 T_1^2} \quad [12]$$

$$rCRB(T_2) = \frac{(\mathbf{F}^{-1})_{3,3}}{\sigma^2 T_2^2}. \quad [13]$$

In this work, we focused on the latter two, since the *PD*, as defined in this work, is modulated by the receive coil sensitivity and provides only a relative measure. The normalization by the variances cancels out the variance in the definition of the Fisher information matrix, and the normalization by the relaxation time is done to best reflect the $T_{1,2}$-to-noise ratio (defined as $T_{1,2}/\sigma_{T_{1,2}}$). In absolute numbers, the noise in the resulting parameter estimations is given by

$$\sigma_{T_{1,2}} \geq \sqrt{rCRB(T_{1,2})} \cdot \sigma \cdot T_{1,2}, \quad [14]$$

where the input standard deviation σ describes the noise level in all the images along the time series, which is assumed to be constant over time.

Optimal Control

Since $\tilde{\vartheta}$ depends only on the RF-pulses, we can treat it as the control parameter for the radial relaxation in Eq. [7]. Thus, we can employ the rich optimal control literature (11, 12) for numerical optimization of the RF pulse train. We used a Broyden-Fletcher-Goldfarb-Shanno (BFGS) algorithm (15) with $rCRB(T_1)$, $rCRB(T_2)$ and $rCRB(T_1) + rCRB(T_2)$ as objective functions. The numerical optimization was based on $\tilde{\vartheta}(\Delta t \cdot n)$ with a discrete step size of $\Delta t = 4.5$ ms and the evaluation points $n \in \{1, 2, \ldots, N_t\}$ with $N_t = 850$. Three Bloch simulations were performed to evaluate the *rCRB*, one for each vector $\mathbf{b}_i$ (Eqs. [8]-[10]). The simulations of $r(\Delta t \cdot n)$, $dr(\Delta t \cdot n)/dT_1$ and $dr(\Delta t \cdot n)/dT_2$ were each based on a two dimensional vector representation, which has been proven to be very efficient (16). The gradient of the objective function with respect to each $\tilde{\vartheta}(\Delta t \cdot n)$ was explicitly calculated.

Since the *rCRB* intrinsically compares a fingerprint to its surrounding in the parameter space, only a single set of relaxation times is necessary for the optimization (c.f. Discussion). Here, we used the relaxation times $T_1 = 781$ ms and $T_2 = 65$ ms, corresponding to the values measured for white matter as reported in (17). All optimizations were initialized with the pattern provided in the original pSSFP paper (10). The inversion pulse at the beginning of the sequence is accounted for by the start value $r_0 = -1$, and is kept fixed during the optimization. All optimizations were performed twice with two different sets of constraints: One using the sequence to exploit the full angular range $0 \leq \tilde{\vartheta} \leq \pi/2$, and one with $0 \leq \tilde{\vartheta} \leq \pi/4$. The latter limits the flip angle to $\alpha \leq \pi/2$, ensuring consistent slice profiles by virtue of the linearity in the small tip-angle approximation (18), and aiding compliance with safety considerations by avoiding high power large flip-angle pulses.

In order to analyze the influence of the optimization parameters, optimizations were performed for $N_t \in \{850, 855, \ldots, 1200\}$ with fixed $T_1 = 781$ ms, $T_2 = 65$ ms and $\Delta t = 4.5$ ms. Similarly, optimizations were performed for $T_1(\text{ms}) \in \{790, 792, \ldots, 930\}$ with fixed $N_t = 850$, $T_2 = 65$ ms and $\Delta t = 4.5$ ms.

Flip angle-, *TR*- and *TE*-Pattern

The discretized, optimized pattern $\tilde{\vartheta}(\Delta t \cdot n)$ can be interpolated or fitted. For a given function $\tilde{\vartheta}(t)$ and varying *TR* and *TE*, the flip angle pattern is given by

$$\alpha_N = \tilde{\vartheta}(TE_{N-1} + \sum_{n=0}^{N-1} TR_n) + \tilde{\vartheta}(TE_N + \sum_{n=0}^{N} TR_n). \quad [15]$$

Note that TR_n and TE_n vary and depend on $\tilde{\vartheta}$ according to the pSSFP theory (10). The first summand denotes the polar angle at the echo time preceding the RF-pulse and this portion of the pulse flips the magnetization to the *z*-axis. The second summand describes the polar angle at the time of the echo succeeding the RF-pulse. Calculating the flip angles with Eq. [15] ensures the magnetization to switch hemispheres by crossing the *z*-axis in order to form the SSFP-type spin echoes. Note that the RF-pulses are subject to a phase increment of π in consecutive pulses.

For simplicity, we approximate the exact solution of the flip angle pattern based on a fixed $TR = 4.5$ ms, which is equivalent to the discretization of the optimization. Thereafter, the final *TR* and *TE* pattern were calculated with Eq. [5] and [7] in Ref. (10).

Sequence Analysis

Three different simulations were performed to analyze the performance of the optimized patterns. The first simulation relates closely to the derived theoretical framework. The spin evolution was calculate for $\log_{10}(T_1/\mathrm{s}) \in \{-1, -0.99, \ldots, 0.75\}$ and $\log_{10}(T_2/\mathrm{s}) \in \{-2, -1.99, \ldots, -0.25\}$ with Eq. [7]. The encoding power of all described sequences was then analyzed by calculating the $rCRB(T_{1,2})$ with Eqs. [12] and [13] for the given parameter space.

The second and third analyses are based on the matching procedures commonly used in MRF (5). For this purpose, a dictionary was calculated for the above-mentioned set of relaxation times with Eqs. [1]-[3]. This simulation also includes the pSSFP-typical *TR* and *TE* variations. Because the dictionary is ℓ_2-normalized, the correlation coefficient β between the dictionary atoms is given by their inner product. In the second analysis, the fingerprint of the optimized set of parameters ($T_1 = 0.781$ s, $T_2 = 0.065$ s) was compared to the entire dictionary. The third analysis compares all dictionary atoms pairwise. A maximum intensity projection was calculated over T_1, as well as over T_2, which provides insights of the correlation along T_2, considering all T_1 values, and vice versa.

In Vivo Experiments

An asymptomatic volunteer's brain was imaged following written informed consent, and according to a protocol approved by our institutional review board. Measurements were performed with the original pSSFP pattern and the patterns that minimize $rCRB(T_1)$, $rCRB(T_2)$ and $rCRB(T_1) + rCRB(T_2)$, limited to $0 \leq \tilde{\vartheta} \leq \pi/4$ (Fig. 3). All experiments were performed on a 3T Skyra scanner (Siemens, Erlangen, Germany). The 16 head elements of the manufacturer's 20 channel head/neck coil were used for signal reception.

At the beginning of the sequence, a secant inversion pulse (19) with a duration of 10.24 ms was applied, followed by a spoiler gradient. The RF-pulses were implemented as slice selective sinc-pulses with a time-bandwidth product of 2 and a duration of 1100 μs.

Spatial encoding was performed with a radial trajectory and a golden angle increment (20). The acquired resolution of the maps is 1 mm $\times$ 1 mm $\times$ 3 mm at a FOV of 256 mm $\times$ 256 mm $\times$ 3 mm. The readout dwell time was set to 2.4 ms and an oversampling factor of 2 was applied. In the current implementation of the experimental setup, and with aforementioned parameters, the timing of the n^{th} readout can be fulfilled if $\min\{TE_n, TR_n - TE_n\} > 2.1$ ms. When this condition cannot be fulfilled, the readout is skipped. Each sequence was run until 840 spokes were acquired, which took 4.38 s in the case of the original pSSFP sequence, 3.86 s for the T_1-optimized sequence, 3.79 s for the T_2-optimized sequence and 3.80 s for the jointly optimized sequence.

The raw data were compressed to 8 virtual receive coils via SVD compression. Thereafter, image reconstruction was performed with the low rank alternating direction method of multipliers (ADMM) approach proposed in (21). The employed dictionaries were computed with Eqs. [1]-[3] and covered the range $T_1(\mathrm{s}) = 0.3 \cdot 1.02^j \; \forall \; j \in \{0, 1, \dots, 152\}$, thus including the range between 300 ms and 6 s in steps of 2%. The dictionaries covered the range of T_2 values between 10 ms and 3 s in steps of 2%, i.e. $T_2(\mathrm{s}) = 0.01 \cdot 1.02^j \; \forall \; j \in \{0, 1, \dots, 289\}$. For simplicity, off-resonance effects were neglected, as well as B_1 inhomogeneities and other complicating factors such as slice profile imperfections and magnetization transfer. The dictionary was compressed to include singular vectors corresponding to the 6 largest singular values resulting from a singular value decomposition. The data consistency step of the ADMM alogrithm was performed with 20 conjugate gradient steps. In order to prevent non-linear effects from impairing the noise assessment, only a single ADMM iteration was performed and no spatial regularization was applied.

Results

Cramér-Rao Bound

The relative Cramér-Rao bounds in Tab. 1 reveal that the T_2 encoding power of the original pSSFP sequence is significantly weaker when compared to T_1. When optimizing for T_1 while exploiting the full range of $0 \leq \tilde{\vartheta} \leq \pi/2$, the $rCRB(T_1)$ is only reduced slightly and, surprisingly, $rCRB(T_2)$ is somewhat reduced as well. When optimizing for T_2, the $rCRB(T_2)$ can be reduced by 81%. However, this optimization results in a considerably larger $rCRB(T_1)$. When optimizing for $rCRB(T_1) + rCRB(T_2)$, a decrease of 70% in $rCRB(T_2)$ is achieved, at almost no cost in $rCRB(T_1)$. Limiting the polar angle to $0 \leq \tilde{\vartheta} \leq \pi/4$ does not change $rCRB(T_1)$ within the indicated precision when optimizing for T_1. The observed $rCRB(T_1)$ also remains similar when optimizing for T_2 only and for T_1&T_2 simultaneously. However, $rCRB(T_2)$ does increase slightly for all three optimizations when limiting the polar angle.

Analysis on the Bloch-Sphere

The $\tilde{\vartheta}$ patterns obtained from the optimizations using the full range of flip angles ($0 \leq \tilde{\vartheta} \leq \pi/2$) are shown in Fig. 2 (b,e,h,k) along with the signal evolution and its derivatives with

		$0 \leq \tilde{\vartheta} \leq \pi/2$			$0 \leq \tilde{\vartheta} \leq \pi/4$		
optimized for	original	T_1	T_2	T_1&T_2	T_1	T_2	T_1&T_2
$rCRB(T_1)$	0.26	0.22	0.77	0.28	0.22	0.47	0.30
$rCRB(T_2)$	1.18	0.97	0.23	0.35	1.22	0.32	0.39
$rCRB(T_1) + rCRB(T_2)$	1.44	1.19	1.00	0.63	1.44	0.79	0.68

Table 1: The relative Cramér-Rao bound is shown for different optimization scenarios. The gray background highlights the objectives that are minimized by the optimal control algorithm.

respect to the relaxation times (c,f,i,l), as well as the magnetization evolution on the Bloch-sphere (a,d,g,j). The original pSSFP pattern (b) inherits strong fluctuations from the original MRF approach (5). On the contrary, the optimized patterns are comparatively smooth (e,h,k). For all optimizations, the magnetization follows a repetitive, circular trajectory after an initial transition phase (d,g,j). In the case of the optimizations for T_1 (Fig. 2d) and T_2 (Fig. 2g), the repetitive trajectory starts at the time when the longitudinal magnetization first reaches the maximum value. In the case of the joint optimization, the magnetization first completes a distinct full loop before the repetitive part of the trajectory starts (Fig. 2j).

When optimizing for T_1, the magnetization first relaxes along the z-axis, providing no significant signal, then it follows a pear shape (Fig. 2d). Thereafter, the entire repetitive trajectory stays close to the origin. This numerical result is in agreement with the intuitive understanding that T_1-relaxation is fastest at small z-values. The repetitive loops exploit the full range of $\tilde{\vartheta}$ and, starting from $r \approx 0$, the magnetization relaxes along the z-axis ($\tilde{\vartheta} \approx 0$), where the relaxation is fastest and purely T_1-dependent. This can be interpreted as a T_1-encoding section, since the measured signal $\tilde{x}$ is negligible. Thereafter, the polar angle increases rapidly until the magnetization reaches the steady-state ellipse, which splits the Bloch-sphere into areas of increasing and decreasing r. From there on, the polar angle decreases slowly, resulting in an approximately constant $\tilde{x}$, while $d\tilde{x}/dT_1$ decreases slightly and $d\tilde{x}/dT_2$ increases substantially (see magnification). This period can be interpreted as a section, in which the T_1-encoding is read out and T_1 is de-correlated from PD and especially T_2. The loop is completed by a section with $\tilde{\vartheta} \approx \pi/2$, where T_2 is encoded and read out, while the magnetization is destroyed such that a new cycle can start. The last cycle is slightly larger and ends shortly after the point of maximal $\tilde{x}$ and $d\tilde{x}/dT_1$.

Optimizing for T_2, the magnetization first relaxes along the $\tilde{x}$-axis (Fig. 2g). The loops of the repetitive part after the zero-crossing also contain sections with $\tilde{\vartheta} \approx 0$ as for the T_1-optimization. However, the loops are considerably larger in this case. T_2 relaxation is strongest at large $\tilde{x}$-values, which necessitates a large r. Thus, intuitively, a large loop enables strong T_2 encoding. However, the optimization results in $\tilde{\vartheta} < \pi/2$ for most of the loop. The magnification in Fig. 2i reveals a piecewise linear decay of $d\tilde{x}/dT_2$, which is presumably optimal and determines the shape of the trajectory on the Bloch-sphere (g). The last loop ends at the steady-state ellipse, which is close to the origin at the particular $\tilde{\vartheta}$.

After the inversion pulse, the trajectory of the combined optimization has a snake-like trajectory (Fig. 2j). This can be understood as a sequence of slight T_2-encoding, followed by a curve similar to the T_1-optimized pear-shaped trajectory (d). Contrary to the optimizations for a single $rCRB$, the combined optimization shows a full distinct loop after crossing the origin and before following the repetitive trajectory, which is of similar shape as the T_2-optimized trajectory. The size of the loop lies in between the sizes of the T_1- and T_2-optimized trajectories, and the decay of $d\tilde{x}/dT_2$ exhibits the same piecewise constant decay as the T_2

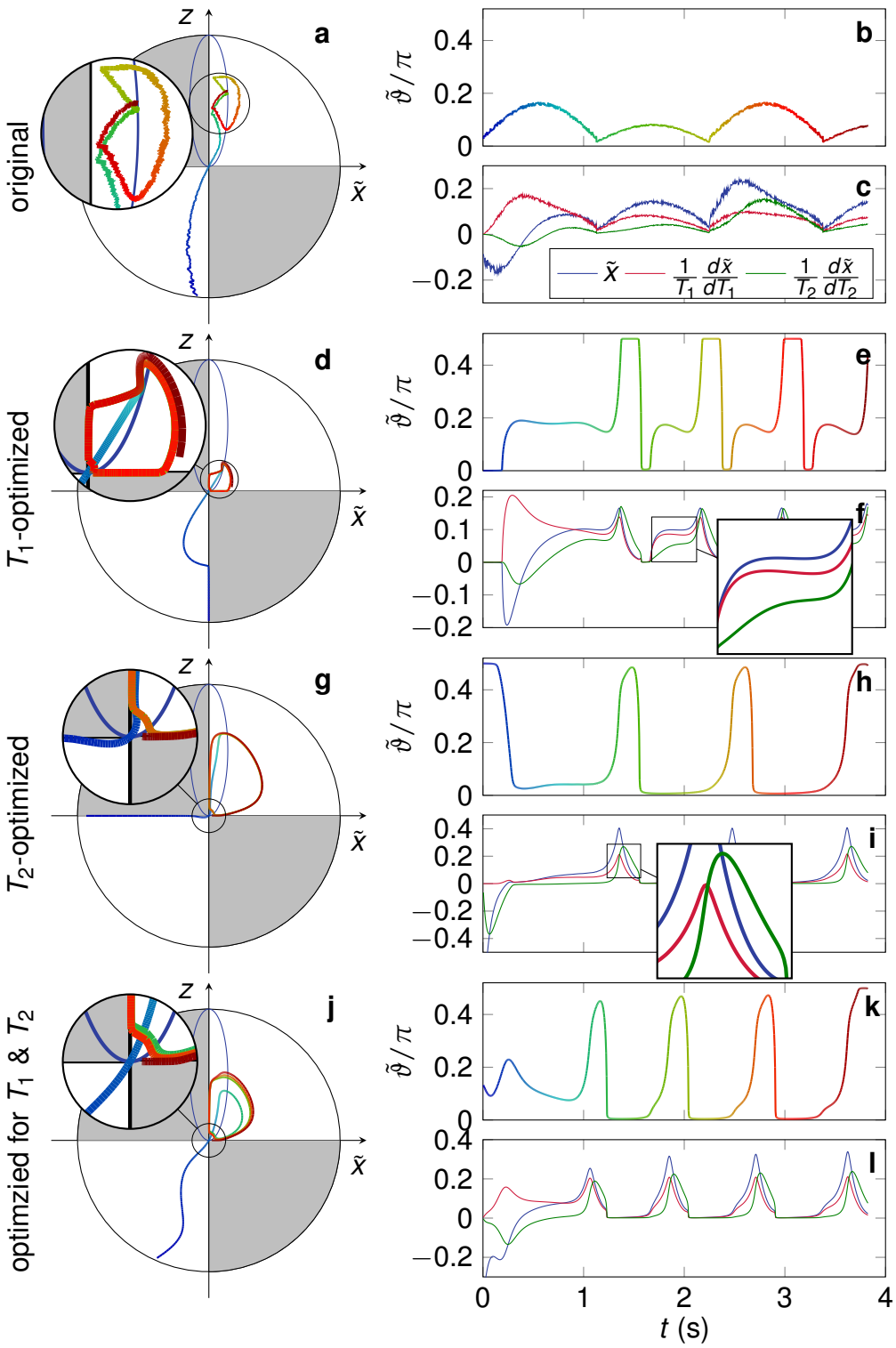

Figure 2: The spin dynamics of optimized excitation patterns is depicted on Bloch-spheres (a,d,g,j) together with the steady-state ellipse (thin blue lines in the upper hemispheres). The excitation angle patterns are shown in (b,e,h,k), with the color scale providing a reference for the trajectories on the Bloch-sphere. The optimized transversal magnetization and its normalized derivatives with respect to the relaxation times are the foundation of computing the relative Cramér-Rao bound and are shown in (c,f,i,l). All excitation patterns were limited to $0 \leq \tilde{\vartheta} \leq \pi/2$.

optimized trajectory. The last cycle ends again at the steady-state ellipse close to the origin.

When limiting the polar angle to $0 \leq \tilde{\vartheta} \leq \pi/4$, the magnetization takes more time to complete a loop, resulting in fewer repetitions (Fig. 3). Surprisingly, the sections with $\tilde{\vartheta} \approx 0$ vanish as well. Instead, the magnetization follows a trajectory between the z-axis and the steady-state ellipse. The trajectories on the Bloch-sphere (d,g,j) illustrate an important feature of all optimized patterns: When the shrinking magnetization crosses the steady-state ellipse (d,g,j), the polar angle decreases rapidly (e,h,k), resulting in an almost perpendicular trajectory on the Bloch-sphere (magnifications in Fig. 3d,g,j). The T_2-optimized trajectory is the only one which does not exploit the full range of $\tilde{\vartheta} \leq \pi/4$. Instead, $d\tilde{x}/dT_2$ exhibits a piecewise linear decay.

The spin dynamics depicted in Fig. 2 and 3 were calculated with Eq. [7] with a constant TR and $TE = TR/2$. In contrast, the dictionaries used for the in vivo experiments were simulations with the full, Cartesian Bloch Equations [1]-[3], and with the TR and TE variations that are required to fulfill the pSSFP conditions. The maximum RMSE of the simulation with Eq. [7] was 1.7% compared to the full simulation with Eqs. [1]-[3] and comprises the approximations used for deriving Eq. [7], as well as the simplistic implementation of the TR and TE variations (c.f. Methods, Section Flip angle-, TR- and TE-Pattern).

Influence of T_{exp}/T_2 and T_1/T_2

So far, the parameters $N_t = 850$, $T_1 = 781$ ms and $T_2 = 65$ ms were fixed for all optimizations. Fig. 4 illustrates the influence of those variables on the T_1-optimized trajectory. As anticipated by Eq. [A5], only their relative size influences the spin dynamics. Optimization results for different $T_{exp} = N_t \cdot \Delta t$ are shown in Fig. 4a,b, while Fig. 4c,d depict optimizations with different T_1 values.

When increasing T_{exp}, the optimized $\tilde{\vartheta}$ is stretched, which leads to slightly larger $\tilde{x}$ values on the outer part of the Bloch-sphere (Fig. 4a,b). Exceeding a certain threshold for T_{exp}, a jump occurs after which four instead of three loops are completed. Directly after the jump, the loops are comparatively small and get larger with further increasing T_{exp}. One can picture the trajectories directly before and after the jump as bounds between which the optimized trajectory is stretched.

Increasing T_1 leads to deformations of the optimized $\tilde{\vartheta}$ pattern (Fig. 4d). A longer T_1 lengthens the inversion recovery phase at the beginning of the experiment and deforms the repetitive part. Especially the sections with small $\tilde{\vartheta}$-values show considerable variations. On the Bloch-sphere, these changes lead to smaller loops with increasing T_1. This compression can be seen in analogy to the steady-state ellipse, which is also squeezed when increasing T_1/T_2 as indicated in Fig. 4c. Note that the number of loops reduces when T_1 is further increased (not shown).

Analysis in the Parameter Space

So far, the *rCRB* was analyzed only at the specific $T_1 = 781$ ms and $T_2 = 65$ ms that were used for the optimization. Fig. 5 analyzes the sequences optimized for these particular parameter values over a larger parameter space, i.e. over a larger range of T_1 and T_2 values, as might be represented in a realistic MRF dictionary. All analyses to follow are based on solutions subject to the constraint $\tilde{\vartheta} \leq \pi/4$, as depicted in Fig. 3. The poor T_2-encoding of

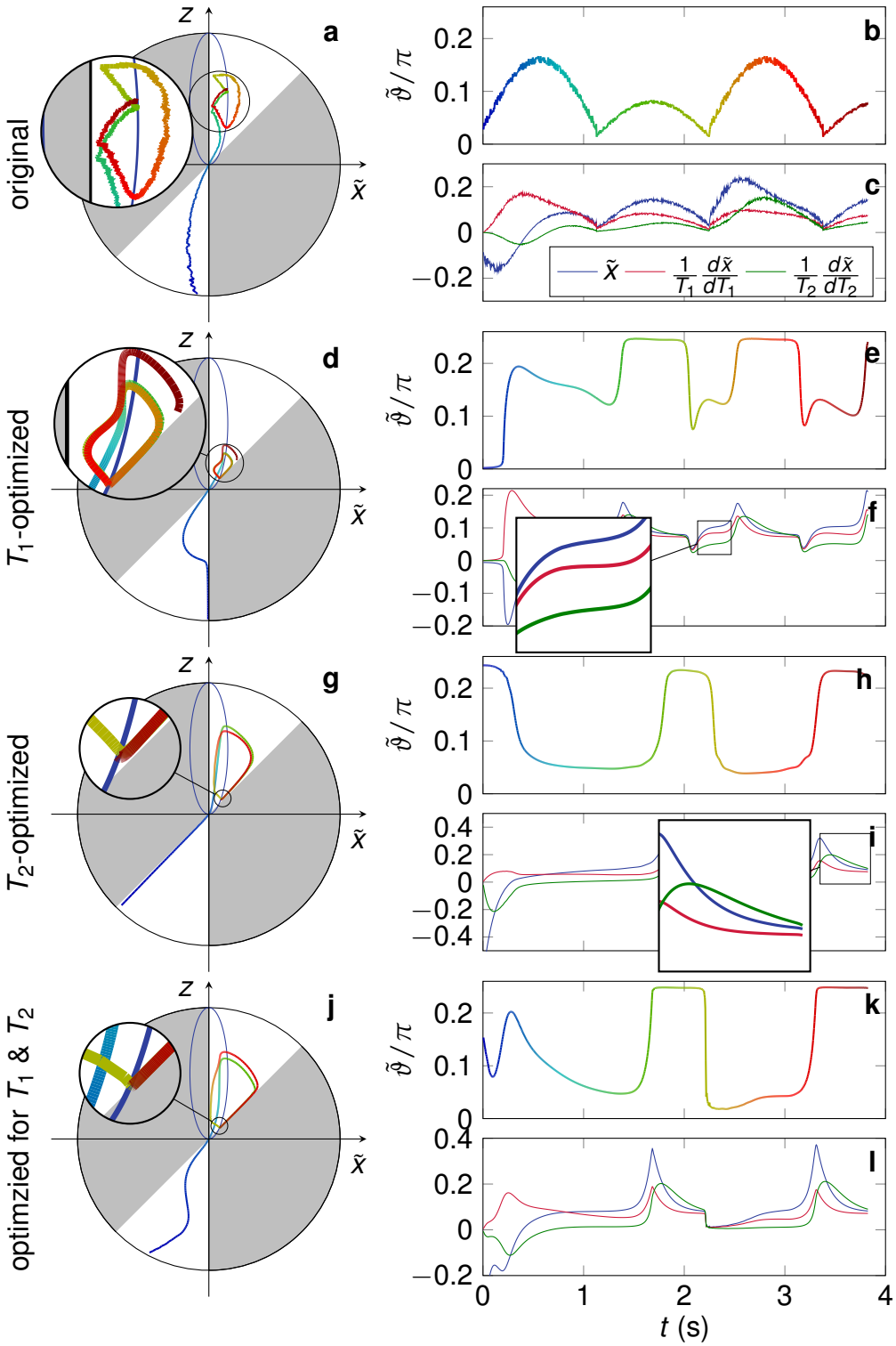

Figure 3: The spin dynamics of optimized excitation patterns with the polar angle limited to $0 \leq \tilde{\vartheta} \leq \pi/4$ *is depicted on Bloch-spheres (a,d,g,j) together with the steady-state ellipse (thin blue lines in the upper hemisphere). The excitation angle patterns are shown in (b,e,h,k), with the color scale providing a reference for the trajectories on the Bloch-sphere. The optimized transversal magnetization and its normalized derivatives with respect to the relaxation times are the foundation of computing the relative Cramér-Rao bound and are shown in (c,f,i,l). These excitation patterns were used for the in vivo experiments.*

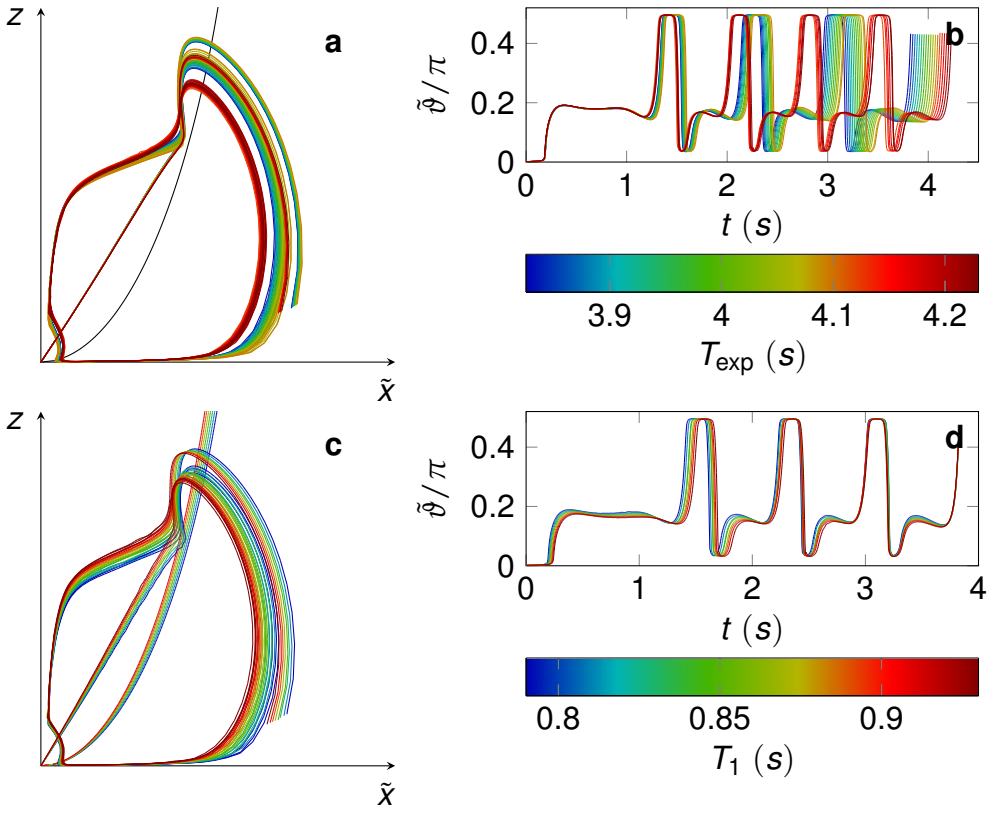

Figure 4: The influence of a varying duration of the experiment (T_{exp}) (a,b) and a varying T_1 (c,d) is analyzed for the case of T_1-optimizations. Note that essentially T_{exp}/T_2 and T_1/T_2 are varied by keeping $T_2 = 65$ ms fixed. Only excerpts of the Bloch-sphere are depicted in (a,c), focusing on the repetitive part of the trajectory. In (c), the steady-state ellipse changes with T_1 and is, therefore, color coded as well.

the original pattern is nicely reflected in a large $rCRB(T_2)$ over the whole parameter space, while $rCRB(T_1)$ is considerably lower over the entire parameter space (note the different color-scales). When optimizing for T_1, $rCRB(T_1)$ is not merely reduced at the optimized set of parameters, which is visualized by the red dot. In fact, the strongest decrease of $rCRB(T_1)$ is achieved at larger T_2 values. When optimizing for T_1, the $rCRB(T_2)$ increases at the relaxation times used for the optimization (Tab. 1), as well as at small T_2-values. However, at large T_2-values, $rCRB(T_2)$ is decreased by the optimization for T_1. Similar observations can be made for the T_2 optimization, where $rCRB(T_2)$ decreases over a large area. Also, the T_2 optimization results in an increased $rCRB(T_1)$ in some areas, including the optimized parameter set, while it results in decreased $rCRB(T_1)$ values in other parts of the parameter space. Optimizing for $rCRB(T_1) + rCRB(T_2)$, result in large improvements for both parameters and in most areas of the parameter space, especially for large T_2-values.

Fig. 6 and 7 analyzes the correlation coefficients, as used to reconstruct the quantitative maps (5, 21). Fig. 6 depicts the correlation between the fingerprint corresponding to the T_1 and T_2 values used during the optimization (red square) and the other fingerprints in the dictionary. These results are in good agreement with the *rCRB* plots shown in Fig. 5. When using the original pattern, the correlation quickly drops along the T_1 dimension, indicating effective encoding, whereas large correlation coefficients are observed even for long T_2-relaxation times, indicating poor T_2 encoding. Even when optimizing for T_1, the T_2 encod-

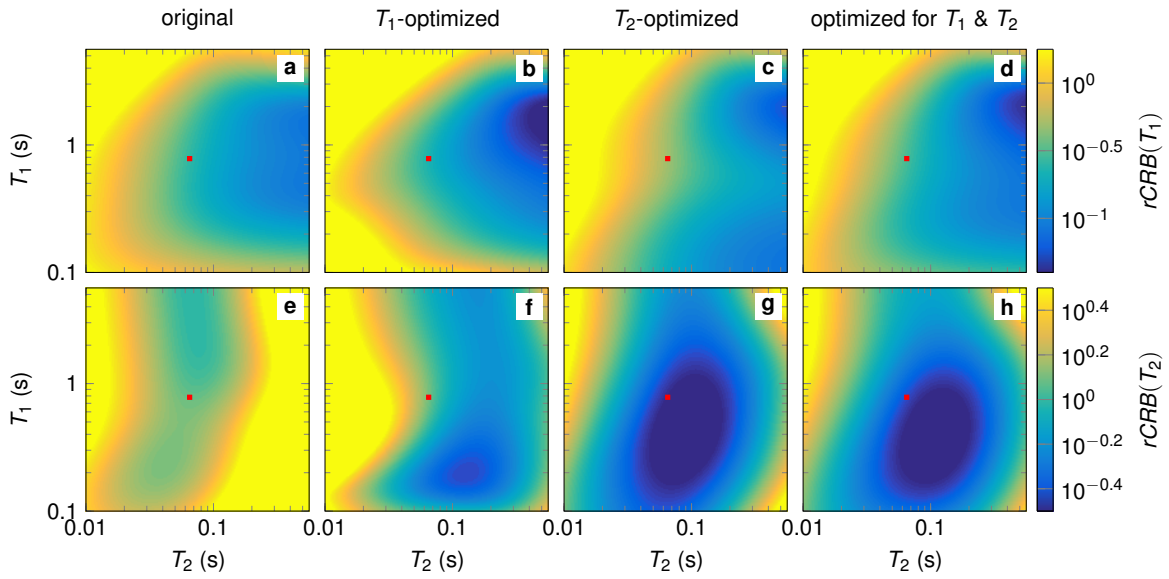

Figure 5: The performance of the patterns optimized with $0 \leq \tilde{\vartheta} \leq \pi/4$ *(Fig. 3) is illustrated through plots of the relative Cramér-Rao bounds, which provide a lower bound for the noise in the retrieved relaxation times. All patterns were optimized for* $T_1 = 781$ *ms and* $T_2 = 65$ *ms, as indicated by the red square, and were tested for the entire parameter space in a sample MRF dictionary. Note the different color scales for* $rCRB(T_1)$ *and* $rCRB(T_2)$*, and the logarithmic scale in all three dimensions.*

ing is improved, as it is made evident by the more rapid decrease in correlation values for large T_2 values. Optimizing for T_2 helps to de-correlate the different entries along the T_2 dimension, at the cost of slightly increased correlation along the T_1 dimension, and optimizing for $rCRB(T_1) + rCRB(T_2)$ results in a similar trade-off between both parameters.

Fig. 7 shows maximum intensity projections of the full correlation matrix among all fingerprints in the dictionary. These projections can be understood as the worst case correlations for a single parameter under consideration of all values of the other parameter. The generally larger $rCRB(T_2)$ compared to $rCRB(T_1)$ is reflected by the correlation coefficients, which are scaled equally. Fig. 7b reveals an improvement around the optimized parameter (red lines). However, this optimization leads to considerably larger correlations for both very small and very large T1 values, which is in agreement with the large $rCRB(T_1)$ for these

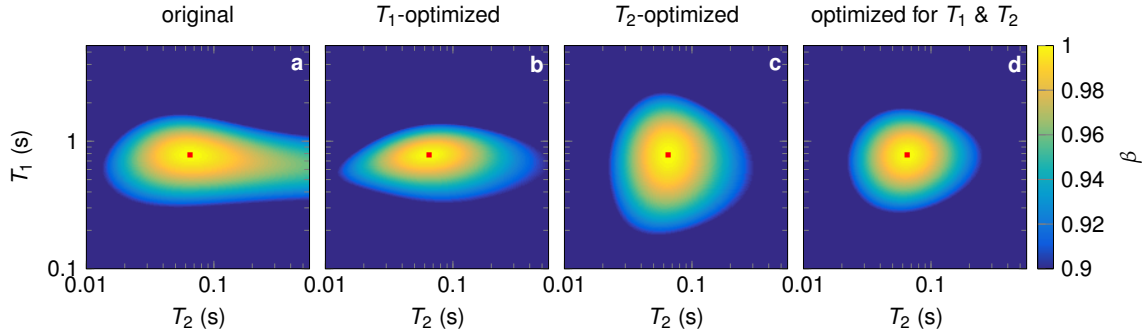

Figure 6: The performance of the patterns optimized with $0 \leq \tilde{\vartheta} \leq \pi/4$ *(Fig. 3) is illustrated through plots of the correlation of the fingerprint using the optimization parameters* $T_1 = 781$ *ms and* $T_2 = 65$ *ms (red square) with the rest of the parameter space.*

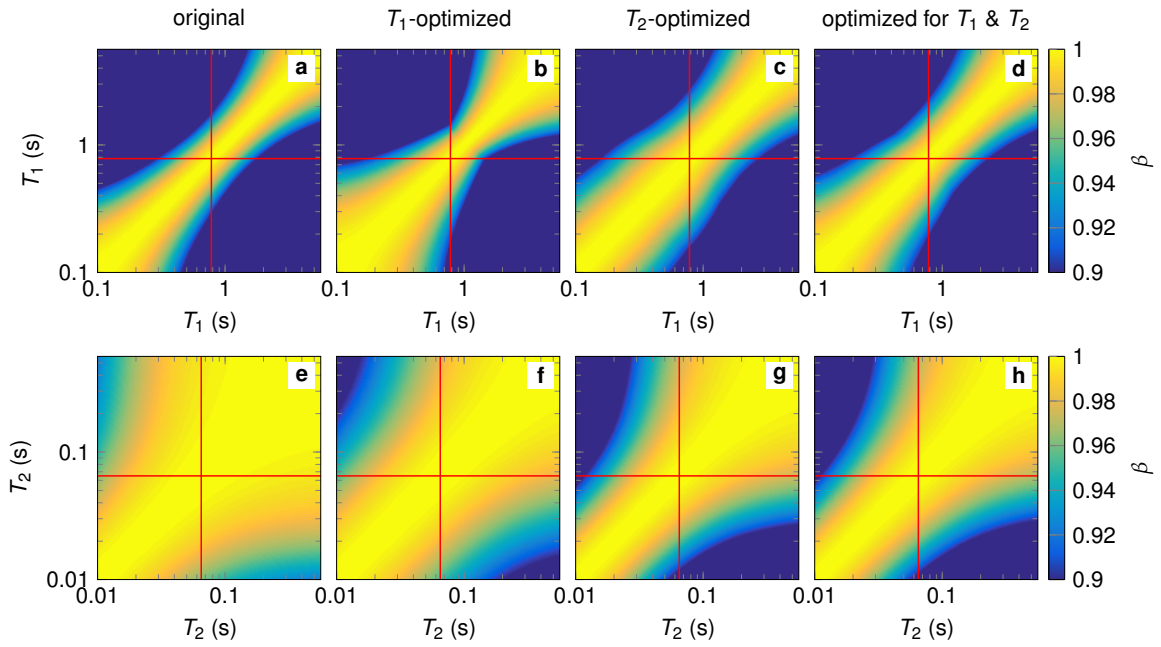

Figure 7: The performance of the patterns optimized with $0 \leq \tilde{\vartheta} \leq \pi/4$ *(Fig. 3) is depicted through plots of the correlation coefficient. The correlation matrix was calculated for the entire parameter space. Thereafter, a maximum intensity projection was performed along the* T_2*- (a-d) and the* T_1*-dimension (e-h), respectively. The result can be understood as the worst case correlations for a single parameter under consideration of all values of the other parameter. The red lines indicates the set of parameters used for optimizing the patterns.*

values (Fig. 5b). The correlations in the T_2-dimension are improved by all optimizations, confirming the results in Fig. 5.

In Vivo Experiments

Fig. 8 depicts quantitative maps acquired with the patterns shown in Fig. 3 and with one radial k-space spoke acquired in each time frame. The total scan time was approximately 3.8 s for each of the four experiments. The excellent T_1 encoding of the original pSSFP pattern translates into T_1 maps with relatively low noise, whereas its poor T_2 encoding power translates into a very noisy map. The maps acquired with the T_1-optimized sequence show minor improvements in T_1, which is also reflected in the standard deviation measured over a region of interest in the frontal cortex (Tab. 2). At the same time, the noise in the T_2-map increases. When optimizing for T_2, the noise in T_1 increases slightly, while the standard deviation of T_2 is reduced by 58%. The maps acquired with the jointly optimized sequence shows a reduced standard deviation for both parameters (Tab. 2).

Systematic deviations can be noted in the measured relaxation times and the proton density (Tab. 2). These variations are most likely caused by slice-profile imperfections and magnetization transfer (22), which are not addressed in the present work.

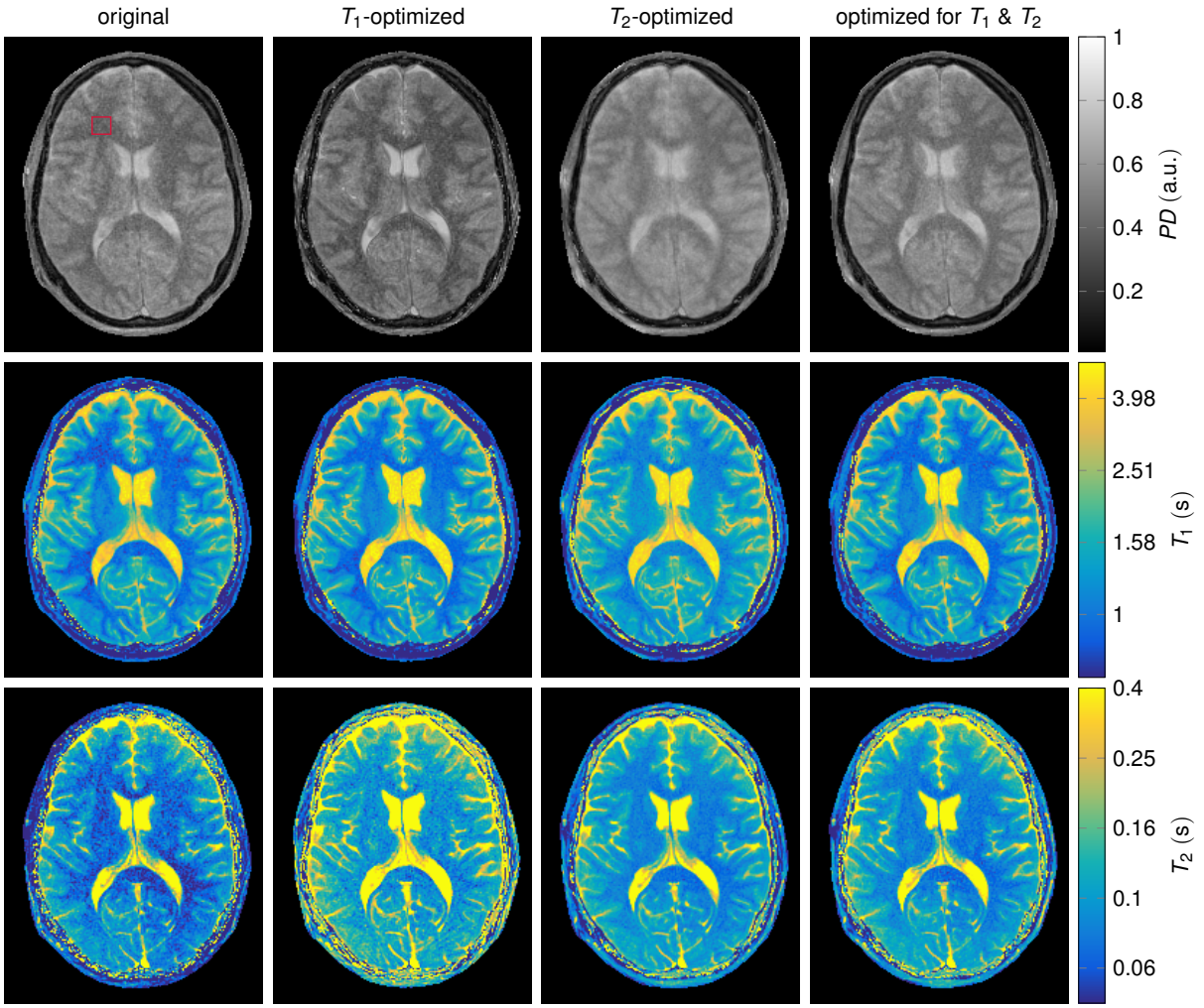

Figure 8: The in vivo data were acquired with the excitation patterns depicted in Fig. 3. The parameter maps have an in-plane resolution of 1 *mm and were reconstructed from 840 radial spokes. The scan time varied slightly for the different acquisitions, and was approximately* 3.8 *s. Note the logarithmic scale of the T_1 and T_2 color map. The red rectangle indicates the region of interest used for calculating the mean and standard deviation listed in Tab. 2.*

		$0 \leq \tilde{\vartheta} \leq \pi/4$		
optimized for	original	T_1	T_2	T_1&T_2
T_1 (s)	0.854 ± 0.079	0.914 ± 0.066	1.086 ± 0.085	0.918 ± 0.066
T_2 (s)	0.069 ± 0.012	0.094 ± 0.016	0.080 ± 0.005	0.082 ± 0.007

Table 2: The measured relaxation times within a region of interest in the frontal white matter are shown. The data were acquired with the pulse sequences depicted in Fig. 3, and the corresponding images are shown in Fig. 8.

Discussion

in order to create the best possible MRF sequence, one might need to jointly optimize not only the complex-valued RF-pulse train but also *TR*, *TE*, spoiling gradients and k-space trajectories in each *TR*. However, this would result in a very complex model with an unwieldy and highly non-convex optimization landscape, impractical for numerical optimization. Therefore, we separate encoding of the quantitative parameters from spatial encoding in our analysis. This paper's focus is on the first part, specifically tailored to pSSFP sequences. The second part will be the subject of future work.

The optimization of SSFP-based MRF sequences was previously discussed (23). In this work, the flip angle and *TR* patterns were allowed to change freely, which prohibits SSFP-type spin echo formation (13, 10), and could result in erroneous parameter maps. Here, we used this spin echo nature to derive a single first order differential equation (Eq. [7]), which approximates the Bloch equations during pSSFP sequences under the assumption of $TR \ll \{T_1, T_2, \pi/|\omega_z|\}$. This simplified description ensures adherence to the pSSFP conditions (10) and, thus, a benign magnetization response without any additional, non-linear boundary conditions. It also facilitates physical intuition about key drivers of MRF optimization - intuition which might be more challenging to derive by other means.

The derived Eq. [7] describes the spin motion in spherical coordinates, and separates the relaxation processes in the radial direction from the explicit effects of the RF-pulses along the polar angle. We can, therefore, view the polar angle as the control of the relaxation in the radial dimension. The polar angle is numerically optimized on the basis of the optimal control framework (11, 12), and the flip angle is given analytically for a given polar angle pattern. In contrast to explicitly optimizing the flip angle, as is commonly done in RF-pulse design, our approach implicitly ensures adherence to the first pSSFP condition. Further, we showed that the optimal pattern is independent of *TR*, so long as $TR \ll \{T_1, T_2\}$, such that the second and third pSSFP conditions (10) can be fulfilled retrospectively.

The Cramér-Rao bound was used as figure of merit, since it provides a universal lower bound for the noise transfer from a time series of images to the quantitative parameter maps. It also provides the flexibility to tailor the acquisition to, for example, encode T_1, while accounting for correlations in T_2-space. The framework also allows joint optimization of multiple parameters with freely adjustable weights. Here, we optimize the Cramér-Rao bound at a single set of relaxation times. Although the non-linearity of the Bloch-equations could potentially lead to close correlations between sets of parameters that are far apart in the parameter space, we showed that this is not the case here (Fig. 5, 6, 7). In fact, the optimization for a single set of relaxation times resulted in an improved performance over a broad area in the parameter space (Fig. 5). Nevertheless, the optimization framework can also be used to simultaneously optimize multiple sets of parameters to improve the encoding performance over an even broader range of parameters. Note that the Cramér-Rao bound does not predict the actual noise level in the quantitative maps. The ratio of the actual noise level in the maps to the bound is usually referred to as efficiency, which could be used as a measure for the optimality of the k-space pattern and the reconstruction techniques.

The proposed optimizations result in a smoothly varying polar angle, which gives confidence in terms of convergence considering the non-convex space and promises a benign magnetization response (Fig. 2, 3). Moreover, polynomial fitting can be used to determine a continuous function $\tilde{\vartheta}(t)$, which could be used to provide precomputed optimized pattern with the flexibility for protocol adjustments, in particular for changes in *TR*, without the need

to rerun the optimization. After an initial inversion recovery period, the magnetization pursues a repetitive trajectory, which allows one to flexibly lengthen the experiment, if required for higher resolution, higher SNR etc. Lengthening the sequence by a full cycle can be implemented by a straightforward concatenation. However, when the duration of the experiment is varied by less than a full cycle, the optimized pattern is slightly distorted, as indicated by Fig. 4. These distortions are smooth, and polynomial fitting could provide a general description of the optimized solution for different durations. Note that the entire equation of motion (Eq. [A5]) depends only on the ratios T_1/T_2 and T_{exp}/T_2. Changing the ratio T_1/T_2 also results in smooth changes of the excitation pattern.

The optimized trajectories were analyzed on the Bloch-sphere (Fig. 2, 3). All optimized RF pulse trains show a series of repetitive loops in which the polar angle drops abruptly, once the shrinking magnetization crosses the steady-state ellipse (see magnifications in Fig. 2d,g,j and Fig. 3d,g,j). A key difference between T_1- and T_2-optimized trajectories is the size of the repetitive loops. The T_1-optimized trajectories reveal characteristic sections, which provide negligible signal, but exhibit a pure T_1-relaxation (Fig. 2). Shrinking magnetization follows one of two trajectories: T_1 optimizations (Fig. 2d-f, 3d-f) and the combined optimization of T_1&T_2, limited to $0 \leq \tilde{\vartheta} \leq \pi/4$ (Fig. 3j-l), exploit the maximum polar angle for fast shrinkage. All T_2-optimized trajectories (Fig. 2g-i, 3g-i), and the combined optimization with $0 \leq \tilde{\vartheta} \leq \pi/2$ (Fig. 2j-l), do not exploit the full range, but instead choose a trajectory that implies a linear decay of the derivative $d\tilde{x}/dT_2$.

The current implementation of the optimization uses the limits $-1 \leq r(t) \leq 1$ and $0 \leq \tilde{\vartheta}(t) \leq \pi/2$. This unusual definition was chosen on the basis of the spin physics in (p)SSFP sequences. The definition deliberately prohibits magnetization from revisiting the southern hemisphere after passing through the origin, such that the RF-pulses can be implemented without major violations of the small tip-angle approximation. Nevertheless, if desired, this limitation could be overcome by simply changing the limits to $0 \leq r(t) \leq 1$ and $0 \leq \tilde{\vartheta}(t) \leq \pi$. However, this would change the optimization landscape, and the convergence behavior might be impaired. In this work we further limited the polar angle to $0 \leq \tilde{\vartheta} \leq \pi/4$, and thereby the flip angle to $\alpha \leq \pi/2$, for practical implementation. The proposed framework has the flexibility to incorporate additional constraints, such as the total power deposition, which can be helpful when dealing with the increased specific absorption rates observed at higher field strengths.

The present work focuses on optimizations with respect to noise within the model of the standard Bloch equation. The in vivo data shown in Fig. 8 are still corrupted by systematic errors such as imperfect slice profiles, B_0- and B_1-inhomogeneities, and magnetization transfer effects. The first three problems can be corrected during the reconstruction process (5, 7, 8, 24), and it may be possible to also address magnetization transfer effects using a multi pool model (22). Future work will include optimizations that incorporate B_0- and B_1-inhomogeneities, as well as magnetization transfer affects in order to minimize correlations between these parameters and the relaxation times. Future work will also include the optimization of the k-space trajectory on the basis of optimized excitation patterns.

Conclusion

Describing the spin dynamics in spherical coordinates provides insights into the behavior of the spin dynamics in balanced non-steady-state sequences. For the special case of pseudo-SSFP sequences, the Bloch equations can be simplified substantially, while also ensuring adherence to the pSSFP conditions. In this simplified description, the polar angle can be viewed as a control parameter, which provides indirect access to the relaxation in the radial direction. Numerically optimizing the T_1 and T_2 encoding on this basis resulted in pSSFP-based MR Fingerprinting sequences with smooth RF-patterns. We showed that these optimized RF-pulse trains enable quantitative parameter mapping with superior SNR, and allow for an intuitive analysis of the T_1 and T_2 encoding process.

Appendix

Angular Relaxation

In the following, we assess the relaxation along the dimension of the polar angle ϑ in the case of pSSFP sequences. The initial state is given by r_0, ϑ_0 or $x_0 = r_0 \sin\vartheta_0, z_0 = r_0 \cos\vartheta_0$. For the case of free relaxation (in the absence of RF-pulses) we can derive a closed form solution of the Bloch equation [5] based on the Cartesian Bloch equations [1], [3]:

$$\begin{aligned}\vartheta(t) &= \cot^{-1}\left(\frac{z(t)}{x(t)}\right)\\ &= \cot^{-1}\left(\frac{1-(1-z_0)\exp(-t/T_1)}{x_0\exp(-t/T_2)}\right)\\ &= \cot^{-1}\left(\frac{1-\exp(-t/T_1)}{r_0\sin\vartheta_0\exp(-t/T_2)} + \cot\vartheta_0\frac{\exp(-t/T_1)}{\exp(-t/T_2)}\right).\end{aligned} \qquad \text{[A1]}$$

This equation of motion can be approximated by a 3rd order Taylor expansion around $\vartheta_0 = 0$:

$$\vartheta(t) \approx \vartheta_0\frac{\exp(-t/T_2)}{\exp(-t/T_1)+(1-\exp(-t/T_1))/r_0}. \qquad \text{[A1']}$$

pSSFP sequences rely on short repetition times, such that we can assume $1-\exp(-t/T_1) \ll r_0$ for $t \leq TR$, and we can simplify this equation further to

$$\vartheta(t) \approx \vartheta_0\frac{\exp(-t/T_2)}{\exp(-t/T_1)} \qquad \text{[A1"]}$$

Assuming $\vartheta_0 > 0$ without loss of generality, we can calculate the evolution of magnetization during a gedankenexperiment with the sequence $\{TR/2, (-2\vartheta_0-\Delta), TR, (2\vartheta_0+3\Delta), TR/2\}$. In the absence of relaxation, each RF-pulse mirrors the magnetization at the y-axis and increments ϑ by $\Delta \ll \vartheta_0$, such that the resulting angle after $2TR$ is $\vartheta_0 + 2\Delta$. On the basis of this slowly and monotonously varying ϑ, the effect of relaxation along the angular dimension is assessed. After the time $TR/2$ of relaxation and an RF-pulse with an integral of $-(2\vartheta_0+\Delta)$, the magnetization is given by

$$\vartheta^+(TR/2) = \vartheta_0 \cdot c - (2\vartheta_0+\Delta) \qquad \text{[A2]}$$

with $c = \exp(-TR/2 \cdot (1/T_2 - 1/T_1))$. The superscript $'+'$ indicates the magnetization after the instantaneous RF-pulse. At the end of this hypothetical pulse sequence, the magnetization is given by

$$\begin{aligned}\vartheta(2TR) &= \vartheta_0 \cdot c^4 - (2\vartheta_0 + \Delta) \cdot c^3 + (2\vartheta_0 + 3\Delta) \cdot c \\ &= \vartheta_0 \left(1 + (c-1)^4 + 2(c-1)^3\right) + \Delta \left(2 - (c-1)^3 - 3(c-1)^2\right)\end{aligned} \quad [A3]$$

Assuming $TR \ll \{T_1, T_2\}$, we can approximate $c \approx 1$, such that the higher order damping terms can be neglected. It follows that

$$\vartheta(2TR) \approx \vartheta_0 + 2\Delta. \quad [A4]$$

Consequently, relaxation along the dimension of the polar angle can be neglected when staying within the above-mentioned limits.

Dimensionless Bloch Equation for pseudo-SSFP Sequences

To highlight its dependencies, Eq. [7] can be multiplied by T_1. Substituting $t \to \tau = t/T_2$ and defining $\dot{r}(\tau) = dr(\tau)/d\tau$, the chain rule results in

$$\frac{T_1}{T_2}\dot{r}(\tau) = \cos\tilde{\vartheta}(\tau) - r(\tau)\cos^2\tilde{\vartheta}(\tau) - \frac{T_1}{T_2}r(\tau)\sin^2\tilde{\vartheta}(\tau), \quad [A5]$$

which demonstrates that the spin dynamics depend only on the relative, dimensionless variables T_1/T_2 and t/T_2.

Acknowledgements

The Authors would like to thank Steffen Glaser, Quentin Ansel and Dominique Sugny for fruitful discussions, and for giving insights into their optimal control implementation.

This work was supported in part by the research grants NIH/NIBIB R21 EB020096 and NIH/NIAMS R01 AR070297, and was performed under the rubric of the Center for Advanced Imaging Innovation and Research (CAI2R, www.cai2r.net), a NIBIB Biomedical Technology Resource Center (NIH P41 EB017183).

References

[1] A P Crawley and R M Henkelman. A comparison of one-shot and recovery methods in T1 imaging. *Magnetic Resonance in Medicine*, 7(1):23–34, 1988.

[2] Hai-Ling Margaret Cheng and Graham A Wright. Rapid high-resolution T1 mapping by variable flip angles: Accurate and precise measurements in the presence of radiofrequency field inhomogeneity. *Magnetic Resonance in Medicine*, 55(3):566–574, 2006.

[3] Sean C L Deoni, Brian K. Rutt, and Terry M. Peters. Rapid combined T1 and T2 mapping using gradient recalled acquisition in the steady state. *Magnetic Resonance in Medicine*, 49(3):515–526, 2003.

[4] Sean C L Deoni, Terry M. Peters, and Brian K. Rutt. Determination of Optimal Angles for Variable Nutation Proton Magnetic Spin-Lattice, T1, and Spin-Spin, T2, Relaxation Times Measurement. *Magnetic Resonance in Medicine*, 51(1):194–199, 2004.

[5] Dan Ma, Vikas Gulani, Nicole Seiberlich, Kecheng Liu, Jeffrey L. Sunshine, Jeffrey L. Duerk, and Mark A. Griswold. Magnetic resonance fingerprinting. *Nature*, 495(7440):187–192, 2013.

[6] Jesse I. Hamilton, Anagha Deshmane, Stephanie Hougen, Mark Griswold, and Nicole Seiberlich. Magnetic Resonance Fingerprinting with Chemical Exchange (MRF-X) for Quantification of Subvoxel T1, T2, Volume Fraction, and Exchange Rate. In *Proc. Intl. Soc. Mag. Reson. Med. 23*, page 329, 2015.

[7] Guido Buonincontri and Stephen J. Sawiak. MR fingerprinting with simultaneous B1 estimation. *Magnetic Resonance in Medicine*, 76(4):1127–1135, 2016.

[8] Martijn A Cloos, F Knoll, T Zhao, K. Block, M. Bruno, CG Wiggins, and Daniel K. DK Sodickson. Multiparamatric imaging with heterogenous radiofrequency fields. *Nature Communication*, 7(12445):doi:10.1038/ncomms12445, nov 2016.

[9] Mike Davies, Gilles Puy, Pierre Vandergheynst, and Yves Wiaux. A Compressed Sensing Framework for Magnetic Resonance Fingerprinting. *SIAM Journal on Imaging Sciences*, 7(4):27, dec 2014.

[10] Jakob Assländer, Steffen J. Glaser, and Jürgen Hennig. Pseudo Steady-State Free Precession for MR-Fingerprinting. *Magnetic Resonance in Medicine*, 77(3):1151–1161, 2017.

[11] S Conolly, D Nishimura, and A Macovski. Optimal control solutions to the magnetic resonance selective excitation problem. *IEEE Transactions on Medical Imaging*, 5(2):106–115, 1986.

[12] Thomas E Skinner, Timo O Reiss, Burkhard Luy, Navin Khaneja, and Steffen J Glaser. Application of optimal control theory to the design of broadband excitation pulses for high-resolution NMR. *Journal of Magnetic Resonance*, 163(1):8–15, 2003.

[13] Klaus Scheffler and Jürgen Hennig. Is TrueFISP a gradient-echo or a spin-echo sequence? *Magnetic Resonance in Medicine*, 49(2):395–397, feb 2003.

[14] Jürgen Hennig, Oliver Speck, and Klaus Scheffler. Optimization of signal behavior in the transition to driven equilibrium in steady-state free precession sequences. *Magnetic Resonance in Medicine*, 48(5):801–809, 2002.

[15] P. De Fouquieres, S. G. Schirmer, S. J. Glaser, and Ilya Kuprov. Second order gradient ascent pulse engineering. *Journal of Magnetic Resonance*, 212(2):412–417, 2011.

[16] Jorge L. Neves, Björn Heitmann, Navin Khaneja, and Steffen J. Glaser. Heteronuclear decoupling by optimal tracking. *Journal of Magnetic Resonance*, 201(1):7–17, 2009.

[17] Yun Jiang, Dan Ma, Nicole Seiberlich, Vikas Gulani, and Mark A. Griswold. MR fingerprinting using fast imaging with steady state precession (FISP) with spiral readout. *Magnetic Resonance in Medicine*, 74:1621–1631, 2015.

[18] D. I. Hoult. The solution of the bloch equations in the presence of a varying B1 field-An approach to selective pulse analysis. *Journal of Magnetic Resonance (1969)*, 35(1):69–86, 1979.

[19] M S Silver, R I Joseph, and D I Hoult. Selectiv spin inversion in nuclear magnetic resonance and coherence optics through an exact solution of the Bloch-Riccati equations. *Phys Rev*, A31(4):2753–2755, 1985.

[20] Stefanie Winkelmann, Tobias Schaeffter, Thomas Koehler, Holger Eggers, and Olaf Doessel. An Optimal Radial Profile Order Based on the Golden Ratio for Time-Resolved MRI. *IEEE Transactions on Medical Imaging*, 26(1):68–76, jan 2007.

[21] Jakob Assländer, Martijn A Cloos, Florian Knoll, Daniel K Sodickson, Jürgen Hennig, and Riccardo Lattanzi. Low Rank Alternating Direction Method of Multipliers Reconstruction for MR Fingerprinting. *Magnetic Resonance in Medicine*, page 10.1002/mrm.26639, 2017.

[22] T Hilbert, F Knoll, T Zhao, K Block, J Thiran, G Krueger, T Kober, D Sodickson, and M Cloos. Magnetic Resonance Fingerprinting: Mitigating the Bias in the Quantification of T1 and T2 Caused by Macromolecules. In *Radiological Society of North America 2016 Scientific Assembly and Annual Meeting*, page archive.rsna.org/2016/16010335.html, 2016.

[23] Bo Zhao, Justin P Haldar, Kawin Setsompop, and Lawrence L Wald. Optimal Experiment Design for Magnetic Resonance Fingerprinting. In *Engineering in Medicine and Biology Society (EMBC), IEEE 38th Annual International Conference of the*, number 1, pages 453–456, 2016.

[24] Dan Ma, Simone Coppo, Yong Chen, Debra F. McGivney, Yun Jiang, Shivani Pahwa, Vikas Gulani, and Mark A. Griswold. Slice profile and B1 corrections in 2D magnetic resonance fingerprinting. *Magnetic Resonance in Medicine*, 00:1–9, 2017.